RSC Advances

PAPER

Cite this: *RSC Adv.*, 2025, **15**, 9430

A highly stretchable, self-adhesive, antimicrobial conductive hydrogel with guar gum/acrylic acid/MXene@AgNPs for multifunctional wearable sensors and electromagnetic interference shielding†

Tongle Pu,[a] Changgeng Li,[b] Lin Yang,[a] Xiu-zhi Tang,[c] Yunjun Ruan[a] and Tong Guo *[a]

Multifunctional conductive hydrogels have attracted extensive attention in the fields of biomedicine and health monitoring. However, integrating excellent stretchability, self-adhesion, sensitive sensing, electromagnetic interference (EMI) shielding, and antibacterial properties into conductive hydrogels for wearable sensor applications remains a significant challenge. In this study, a multifunctional conductive hydrogel (GAMA) was prepared by incorporating MXene@Ag nanoparticles (AgNPs) as conductive fillers, which were uniformly dispersed within a dual-network structure of guar gum/acrylic acid. Serving as conductive agents, reinforcing fillers, and antibacterial components, MXene@AgNPs enable the GAMA hydrogel to achieve multifunctional integration and balanced performance. The GAMA hydrogel exhibits outstanding mechanical performance with a tensile strength of 97 kPa and elongation at a break of 850%, self-adhesion (21.5 kPa), and high conductivity (14.04 mS cm^{-1}). Additionally, we employed this hydrogel as a flexible strain sensor to monitor human motion, achieving high sensitivity (gauge factor (GF) of 6.48 at 300% strain). The *in situ* synthesis of AgNPs on MXene nanosheets enhances polarization and interfacial losses of electromagnetic waves, endowing the hydrogel with an EMI shielding effectiveness of 34.5 dB. Furthermore, comprehensive biocompatibility evaluations confirm its excellent antibacterial performance, hemocompatibility, and cytocompatibility. Therefore, these properties endow the multifunctional GAMA hydrogel with great potential for applications in wearable sensors for human motion monitoring and EMI shielding.

Received 7th January 2025
Accepted 8th March 2025

DOI: 10.1039/d5ra00159e

rsc.li/rsc-advances

1 Introduction

In recent years, flexible wearable electronic devices have attracted increasing attention in applications such as electronic skin,[1,2] human motion monitoring,[3–5] and soft robotics.[6,7] In addition, as the demand for enhanced functionalities in these devices continues to grow across various sectors, the development of multifunctional integration has become crucial for advancing high-performance flexible wearable electronics.[8,9] For instance, owing to superior biocompatibility, structural similarity to natural soft tissues, and excellent electrical conductivity, conductive hydrogels are promising candidates for flexible wearable sensors.[3,10] However, as application environments become more complex, conductive hydrogels must combine excellent electrical conductivity and stress-sensing performance with protective features such as EMI shielding and antibacterial properties. Therefore, the multifunctional integration and balance of conductive hydrogels have become crucial research directions for the development of wearable sensors.

Typically, incorporating conductive fillers such as nanocarbon materials (*e.g.*, graphene, carbon nanotubes) and metal nanoparticles can effectively endow hydrogels with excellent electrical conductivity. However, the mechanical and electrical properties of hydrogels are influenced by the uniform dispersion of conductive fillers.[11,12] MXene, a two-dimensional material similar to reduced graphene oxide (RGO), boasts outstanding electrical conductivity and hydrophilicity. It can disperse uniformly within hydrogels, significantly enhancing their electrical conductivity. Moreover, through the van der Waals interactions between its surface functional groups and polymer chains, MXene improves the mechanical properties of hydrogels. For example, Zhang *et al.*[13] added MXene@CNFs to

[a]College of Big Data and Information Engineering, Guizhou University, Guiyang 550025, China. E-mail: tguo3@gzu.edu.cn
[b]School of Electronic Information, Central South University, Changsha 410083, China
[c]School of Aeronautics and Astronautics, Central South University, Changsha 410083, China

† Electronic supplementary information (ESI) available. See DOI: https://doi.org/10.1039/d5ra00159e

a polyacrylamide/gelatin double-network hydrogel, increasing the tensile strength from the original 80 kPa to 110 kPa. Additionally, due to its good electrical conductivity, this composite hydrogel exhibits a total electromagnetic shielding efficiency (EMI SE) of 33.8 dB at a thickness of 4 mm. More importantly, MXene, as a carrier, can be combined with other functional materials and uniformly dispersed in hydrogels, facilitating multifunctional integration and performance balance.

Considering the safety factors of wearable sensors, the components of conductive hydrogels should be derived from non-toxic or low-toxicity polymeric materials. Natural polymers such as chitosan,[14] alginate,[15] guar gum,[16] gelatin,[17] and nanocellulose[18,19] are particularly suitable for applications in the field of wearable conductive hydrogels due to their excellent biocompatibility and safety. In addition, since hydrogel sensors are directly attached to human skin, there are gaps between the skin and the hydrogel that are similar to the living environment of cells. This situation easily leads to bacterial growth, posing a threat to human health. At the same time, it also shortens the service life of the hydrogel and affects its sensing performance.[20–22] Silver nanoparticles (AgNPs) are widely used in antibacterial composite materials due to their advantages such as broad-spectrum antibacterial properties, durability, and good thermal stability. However, the synthesis of traditional AgNPs relies on chemical reduction methods, such as the reduction of silver nitrate by sodium borohydride. Although this method can rapidly prepare AgNPs, issues such as toxic byproducts, complex synthesis processes, and particle aggregation limit its applications in the fields of biomedicine and flexible electronics. Interestingly, the abundant functional groups on the surface of MXene nanosheets can directly reduce $AgNO_3$, enabling the *in situ* formation of AgNPs. This strategy not only ensures the uniform distribution of AgNPs on the MXene surface but also promotes a synergistic effect that enhances both electrical conductivity and EMI performance. Furthermore, the introduction of AgNPs can significantly improve the antibacterial performance. The released Ag^+ can achieve broad-spectrum and efficient inhibition of various pathogenic bacteria (such as *Staphylococcus aureus*) by mechanisms such as disrupting the bacterial cell membrane, inhibiting enzyme activity, and interfering with DNA replication. Moreover, its long-term effectiveness is superior to that of traditional antibacterial agents.

Herein, we designed a multifunctional hydrogel with electrical conductivity, high stretchability, self-adhesion, and antibacterial properties for applications in wearable sensors and electromagnetic interference (EMI) shielding fields. In detail, MXene loaded with *in situ* generated AgNPs was utilized as a multifunctional filler and incorporated into a mixed solution of natural guar gum and acrylic acid. Subsequently, through *in situ* polymerization, a conductive hydrogel based on a double-network structure of guar gum (GG)/acrylic acid (AA)/MXene@AgNPs (GAMA) was obtained. The GG/AA double-network hydrogel, rich in functional groups, exhibits excellent mechanical properties and self-adhesive properties. Additionally, owing to the van der Waals interactions between MXene and polymer chains, the mechanical properties of the composite hydrogel are further enhanced. Benefiting from the synergistic effect of MXene and AgNPs, the addition of MXene@AgNPs endows GAMA with excellent electrical conductivity, EMI shielding performance, antibacterial properties, and biocompatibility. In addition, when assembled into wearable sensors, the GAMA hydrogel effectively monitored body movements and vocal cord vibrations. Therefore, this study provides new insights into the design and fabrication of multifunctional hydrogels, demonstrating their potential applications in electromagnetic shielding and wearable electronic devices.

2 Materials and methods

2.1 Materials

The GG was purchased from Hefei Bomei Biotechnology Co., Ltd. Ti_3C_2 (MXene) was obtained from Foshan Xinxi Technology Co., Ltd. AA (AR, purity ≥99%), *N*,*N*′-methylene-bis-acrylamide (MBA, AR) and ammonium persulfate (APS, AR, purity ≥98%) were purchased from Aladdin Chemistry Co., Ltd. Silver nitrate was purchased from Sinopharm Chemical Reagent Co., Ltd. *Escherichia coli* (*E. coli*) and *Staphylococcus aureus* (*S. aureus*) were obtained from Guangdong Huankai Microbial Technology Co., Ltd. Human fibroblasts were from the cell bank (Chinese Academy of Sciences). Rabbit serum was obtained from Meryer Biochemical Technology Co., Ltd. All reagents were used directly without further purification.

2.2 Preparation of GAMA hydrogel

First, 0.2 g of MXene powder was added to 10 mL of deionized water and sonicated for 30 min to obtain a uniformly dispersed suspension. Second, 0.1 g of $AgNO_3$ powder was weighed and dissolved in 10 mL of deionized water under magnetic stirring for 10 min. Subsequently, the $AgNO_3$ solution was added drop by drop to the MXene solution, followed by magnetic stirring for 10 min. The mixture was then sonicated for 1 h to yield a homogeneous MXene@AgNPs solution. Next, 0.5 g of GG was added to 20 mL of deionized water and stirred at 60 °C for 30 min until completely dissolved. After stirring for 30 min, 6 mL of AA was added. The mixture was then stirred at 60 °C for another 30 min until it became homogeneous. After that, MXene@AgNPs solution was added to the mixed solution of GG/AA with vigorous stirring at 60 °C for 1 h. Then, 0.014 M of APS initiator and 0.06 M of MBA crosslinker were added to make the mixture homogeneous, and it was quickly transferred to a glass plate mold, and *in situ* polymerization was carried out at 60 °C for 3 h to obtain GAMA hydrogel. The obtained samples obtained were denoted as GAM, $GAMA_1$, and $GAMA_2$ according to the mass of $AgNO_3$ added (0, 0.1 g, 0.2 g). The control samples without MXene nanosheets and AgNPs are denoted as GA.

2.3 Characterization

X-ray diffraction (XRD) patterns of the samples were measured using an X-ray diffractometer (Empyrean PANalytical B. V.). The morphology and elemental profiles of the samples were characterized by field emission scanning electron microscopy (FESEM, SU8010) and Oxford X-Max energy-dispersive X-ray

spectrometer (EDS). Before the characterization, the hydrogel samples were freeze-dried and then fractured in liquid nitrogen to produce fresh cross-sections. The transmission electron microscopy (TEM) were acquired on JEOL JEM-F200. XPS spectra were recorded using an X-ray photoelectron spectrometer (Thermo Scientific K-Alpha+). UV-vis spectra were recorded using a UV-vis spectrophotometer (Shimadzu UV-1900). Fourier transform infrared spectra (FTIR) were recorded using an infrared spectrometer (Nicolet 470, Thermo Scientific) in the wavenumber range of 600 to 4000 cm^{-1}. The tensile properties of the hydrogels were tested by using a universal tensile testing machine (CMT6103, MTS system), the sample size of the tensile specimens was 20 mm × 10 mm × 4 mm, and the loading rate was set at 50 mm min^{-1}. For testing the adhesion strength of the hydrogels, a tensile–shear experiment was constructed using the universal tensile testing machine. The hydrogels were adhered to the surfaces of different substrates, such as wood, polytetrafluoroethylene (PTFE), copper, and glass, with a bonding area of 20 mm × 20 mm. The test was carried out at a tensile rate of 10 mm min^{-1}. The adhesion strength of the hydrogel was calculated by dividing the maximum adhesion force by the initial bonding area. (The structural characterization of MXene@AgNPs, along with the silver release behavior and degradation behavior of the $GAMA_2$ hydrogel, are provided in the ESI†).

2.4 Conductivity tests

The conductivity of hydrogels was measured using an electrochemical workstation (CHI760E, Chenhua). The resistance of hydrogels with dimensions of 30 mm × 20 mm × 4 mm was tested using electrochemical AC impedance spectroscopy in the frequency range of 0.1–100 kHz and an amplitude of 0.1 V. The hydrogels were sandwiched between two copper foils during testing, and the ionic conductivity was calculated using eqn (1):

$$\sigma = \frac{L}{R \times S} \tag{1}$$

where L, R, and S are the thickness of the hydrogel, the impedance value, and the contact area of the hydrogel, respectively.

2.5 Strain sensing tests

The sensing performance of the hydrogel sensor was evaluated using a Chenhua CHI760E electrochemical workstation. The evaluation was carried out with the assistance of a volunteer, and informed consent was obtained for the testing. The changes in real-time resistance of hydrogels with dimensions of 30 mm × 20 mm × 4 mm at different strains were tested by recording the *i–t* curves *via* the electrochemical workstation at a voltage of 2 V. Subsequently, the changes in relative resistance were calculated according to eqn (2):

$$\Delta R = \frac{R_1 - R_0}{R_0} \times 100\% \tag{2}$$

where R_0 is the initial resistance of the hydrogel and R_1 is the resistance of the hydrogel at different strains.

The gauge factor (GF) under tensile strain is calculated from eqn (3):

$$\mathrm{GF} = \left(\frac{R_1 - R_0}{R_0}\right) \times \frac{1}{\varepsilon} \tag{3}$$

where ε is the tensile strain.

2.6 Electromagnetic interference shielding measurements

The EMI shielding performance of the samples was tested in the frequency range of 8.2–12.4 GHz using a vector network analyzer (E5071C, AGILENT). The hydrogel samples were cut into rectangles of 22.86 mm × 10.16 mm × 4 mm. The EMI shielding effectiveness was defined as the logarithmic ratio of incident power to transmitted power. The total SE (SE_T) is the sum of reflection loss (SE_R), absorption loss (SE_A), and multiple reflection loss (SE_M). SE_M can be neglected when SE is greater than 15 dB. The scattering parameters (S_{11}, S_{12}, S_{21}, and S_{22}) are measured, and SE_T, SE_A, and SE_R were calculated according to the following equations:

$$\mathrm{SE_T} = 10 \log\left(\frac{1}{|S_{11}|^2}\right) \tag{4}$$

$$\mathrm{SE_R} = 10 \log\left(\frac{1}{1 - |S_{11}|^2}\right) \tag{5}$$

$$\mathrm{SE_A} = 10 \log\left(\frac{1 - |S_{11}|^2}{|S_{11}|^2}\right) \tag{6}$$

The absorption (A), reflection (R), and transmission (T) coefficients were calculated as:

$$R = |S_{12}|^2 = |S_{21}|^2 \tag{7}$$

$$T = |S_{11}|^2 = |S_{22}|^2 \tag{8}$$

$$A = 1 - R - T \tag{9}$$

2.7 Antimicrobial tests

All materials were sterilized in an autoclave for 30 min at 121 °C. The antimicrobial properties of the hydrogels were evaluated using *Escherichia coli* (Gram-negative bacteria) and *Staphylococcus aureus* (Gram-positive bacteria). First, the hydrogels were sterilized by UV light for 30 min. Subsequently, the hydrogels were placed in test tubes containing 10 mL of bacterial solution (1.0×10^4 CFU mL^{-1}) and the tubes were placed in a shaking incubator for 4 h (37 °C, 200 rpm). After that, the bacterial solution was processed by gradient dilution method, and 100 μL of diluted bacterial solution was added to LB solid medium, coated well, and incubated in a sterile incubator for 24 h. The antibacterial rate was calculated as follows:

$$R = \frac{(A - B)}{A} \times 100\% \tag{10}$$

where R is the antimicrobial rate (%); A is the number of bacteria recovered after 24 h of the blank control hydrogel specimen (CFU/slice); B is the number of bacteria recovered after 24 h of the $GAMA_2$ hydrogel specimen (CFU per slice).

2.8 Cell viability test

The cytotoxicity of the hydrogel on human fibroblasts was evaluated using the CCK-8 assay. The samples were sterilized by ultraviolet irradiation for 30 min. Subsequently, the samples were immersed in DMEM solution at 37 °C for 48 h. Then, the extracts were diluted to different concentrations (0, 0.01, 0.025, 0.05, 0.1, 0.25, 0.5, and 1.0 mg mL^{-1}). Human fibroblasts were seeded into a 96-well plate at a density of 1×10^4 cells per well (100 μL per well). After pre-culturing for 24 h, the medium was replaced with an equal volume of fresh medium containing the extracts. Meanwhile, a blank control (pure DMEM medium) and a negative control (untreated cells) were set up. After 24 h of exposure, 10 μL of 10% CCK-8 reagent was added to each well and incubated in the dark for 1 h. The optical density (OD) value was measured at a wavelength of 450 nm using a microplate reader. The cell viability was calculated using eqn (11):

$$\text{Cell viability } (\%) = \frac{OD_{sample} - OD_{Blank}}{OD_{control} - OD_{Blank}} \times 100\% \quad (11)$$

where OD_{sample}, OD_{Blank}, and $OD_{control}$ are the absorbance values of the sample group, the blank control group, and the negative control group, respectively.

2.9 Hemocompatibility of the $GAMA_2$ hydrogels

The hemocompatibility of the hydrogel was detected by measuring the absorbance of hemoglobin released after the red blood cell (RBC) lysis. First, 5 mL of rabbit blood was collected into an anticoagulant tube. Centrifuge the blood at 1000 rpm for 10 min, then discard the supernatant. Wash the blood cells with physiological saline, and then centrifuge at 1500 rpm for 5 min. Repeat this washing and centrifugation process twice and retain the blood cell pellet. Next, dilute the blood cell pellet to a concentration of 2% (v/v) with PBS. Take 500 μL of the diluted blood cells and mix them at a 1 : 1 volume ratio with 500 μL of hydrogel extracts at different concentrations (10, 50, 100, 200, 500 μg mL^{-1}), PBS (negative control), and distilled water (positive control) respectively. Then, place the mixtures in an environment at 37 °C and let them stand for 1 h. After that, centrifuge at 3500 rpm for 5 min. Transfer the supernatant to a 96-well plate and measure the OD value at 542 nm. The calculation of the hemolysis rate is shown in eqn (12):

$$\text{Hemolysis ratio} = \frac{OD_{sample} - OD_{NC}}{OD_{PC} - OD_{NC}} \times 100\% \quad (12)$$

where OD_{sample}, OD_{NC}, and OD_{PC} are the absorbance values of the sample group, the negative control group, and the positive control group, respectively.

3 Results and discussion

3.1 Synthesis and characterization of hydrogels

The preparation process of GAMA hydrogels is shown in Fig. 1. The MXene nanosheets loaded with AgNPs were incorporated into a mixed solution of GG and AA, and then the dual-network structure of the GAMA conductive hydrogel was fabricated *via in situ* free-radical polymerization. The MXene@AgNPs were uniformly dispersed in the hydrogel and linked to the polymer chains *via* abundant hydrogen bonds.

The microstructure and elemental distribution of the lyophilized GAMA hydrogels were characterized by SEM. As shown in Fig. 2a–c, the hydrogels exhibited a three-dimensional porous structure, with pore diameters of approximately 30 μm in the GA hydrogel and around 10 μm in the GAM and $GAMA_2$ hydrogels. Fig. 2d shows the elemental distribution image of the $GAMA_2$ hydrogel. Ti and Ag are distributed relatively uniformly, indicating the homogeneous dispersion of MXene and AgNPs within the hydrogel. Fig. 2e shows the XRD patterns of MXene@AgNPs powder, pure GA, GAM, and $GAMA_2$ hydrogels. The pure GA hydrogel displayed a low-intensity broad peak at about 27°, indicating an amorphous crystal structure.[23] After the addition of MXene nanosheets to the pure GA gel, a characteristic peak of MXene (002) appeared at 5.5° and the (002) peak of MXene nanosheets shifted to a smaller angle, indicating that the layer spacing of the MXene nanosheets became larger. With the introduction of MXene@AgNPs, three distinct diffraction peaks appeared in the $GAMA_2$ hydrogel at 5.4°, 38.3°, and 44.5°. These peaks corresponded to the (002) facet of the MXene nanosheets and the (111) and (200) facets of the face-centered cubic structure of silver, respectively, suggesting the successful introduction of the AgNPs.

To further elucidate the intermolecular interactions in the $GAMA_2$ hydrogels, the FTIR spectra of the pure GA, GAM, and $GAMA_2$ are presented in Fig. 2f. All three hydrogels exhibited broad peaks at 3450 cm^{-1}, which can be attributed to the absorption of water and the stretching vibration of the –OH group, indicating the formation of hydrogen bonds.[24] The peak associated with C–O stretching vibration was observed at 1699 cm^{-1}, where carbonyl (C═O, hydrogen bond acceptor) and hydroxyl (–OH, hydrogen bond donor) groups can produce a high density of hydrogen bonding.[25] This is in agreement with the broad peak at 3450 cm^{-1}, which suggests the formation of hydrogen bonding between the polymer chains and MXene nanosheets. The XPS spectra of MXene powder, GA, GAM, and $GAMA_2$ hydrogels are demonstrated in Fig. 2g. From these spectra, it can be observed that the peaks corresponding to Ti 2p and F 1s appeared in the XPS curves of the GAM and $GAMA_2$ hydrogels. Additionally, the Ag 3d peaks are observed in the $GAMA_2$ hydrogel, indicating the successful incorporation of MXene and AgNPs, which was further confirmed by the EDS image. The high-resolution spectra of C 1s and O 1s of $GAMA_2$ hydrogels were further analyzed, as shown in Fig. 2h and i. The core energy level spectrum of C 1s had four peak components, C–C/C═C (284.8 eV), C–O (285.4 eV), C–Ti (284 eV), and C═O (289.4 eV), and the core energy level spectrum of O 1s had two

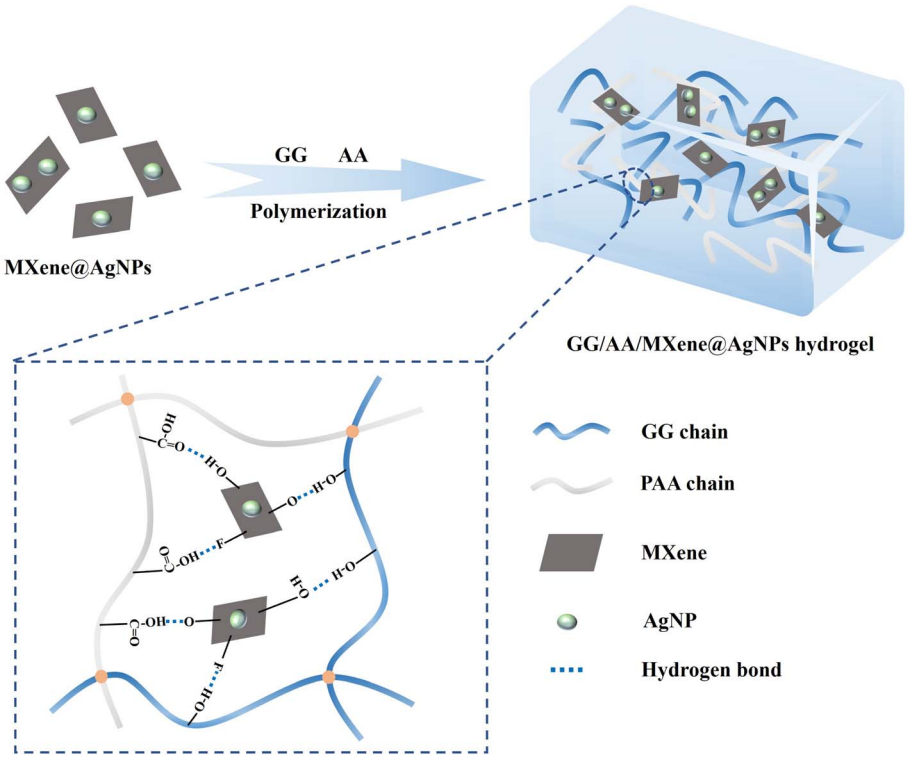

Fig. 1 Schematic illustration for the fabrication of the GAMA hydrogel.

peak components, C–O (532 eV) and C=O (533.3 eV). The strong C signal indicates the presence of abundant hydrophilic groups on the guar and acrylic chains, which provided abundant cross-linking sites in the hydrogel.

3.2 Mechanical properties of hydrogels

Excellent mechanical properties, good elasticity, and high stretchability are essential for hydrogels to govern the applicability of hydrogel sensors. Fig. 3a–c demonstrate the tensile stress–strain curves, strength and elongation, as well as the toughness and elastic modulus of GA, GAM, $GAMA_1$, and $GAMA_2$. The GA hydrogel exhibits poor mechanical properties, with a fracture strain of 567%, a tensile strength of 84.84 kPa, and a relatively low toughness of only 277 kJ m^{-3}. After incorporating MXene nanosheets, the GAM hydrogel demonstrates significantly improved mechanical properties, with a tensile strength of 182 kPa, a fracture strain of 1198%, and a maximum toughness of 1041 kJ m^{-3}, far surpassing those of the GA hydrogel. This enhancement primarily results from the large surface area and abundant polarized functional groups of MXene nanosheets, which facilitate stress transfer to more PAA and GG chains, effectively preventing stress concentration.[13] However, after introducing MXene@AgNPs, the mechanical properties of the $GAMA_1$ hydrogel declined compared to those of the GAM hydrogel, with a fracture strain of 724% and a tensile strength of 103.6 kPa. Moreover, as the AgNPs content increases, the tensile strength of the $GAMA_2$ hydrogel further decreases. This is mainly because AgNPs adhere to the surface of MXene nanosheets, reducing the number of available polarized functional groups. Consequently, the interactions between MXene and both PAA and GG chains weaken, leading to a decline in tensile strength.

Fig. 3d shows the loading–unloading curves of $GAMA_2$ hydrogel under 300% tensile strain for 10 consecutive cycles. The significant hysteresis observed in the first cycle is likely attributed to the extensive breaking of hydrogen bonds, effectively dissipating energy and preserving the integrity of the gel network. After the first cycle of loading, the subsequent hysteresis loops nearly overlapped and the dissipated energy was almost constant, indicating a good cyclic stability. In addition, the hydrogels were also subjected to compression tests. Fig. 3e shows the compression stress–strain curves of the hydrogels with different conductive fillers added. It can be seen that the $GAMA_2$ hydrogel exhibits the highest compression strength of 350 kPa. Fig. 3f shows the compression of $GAMA_2$ hydrogel at 70% strain for 10 cycles at a rate of 10 mm min^{-1}. The hysteresis curve and energy in the first cycle are higher than in subsequent cycles but stabilize with increasing cycle numbers, demonstrating the $GAMA_2$ hydrogel's excellent fatigue resistance and rapid deformation recovery. As illustrated in Fig. 3g and h, the $GAMA_2$ hydrogel exhibits exceptional stretchability, extending over 10 times its original length without rupture. Moreover, under the finger pressure, the hydrogel can be restored to its original shape without any damage after it is released from the finger, indicating that the hydrogel exhibits excellent shape recovery.

3.3 Adhesion properties of hydrogels

Self-adhesion ensures a tighter interface between the conductive hydrogel and the target surface, thereby maintaining the

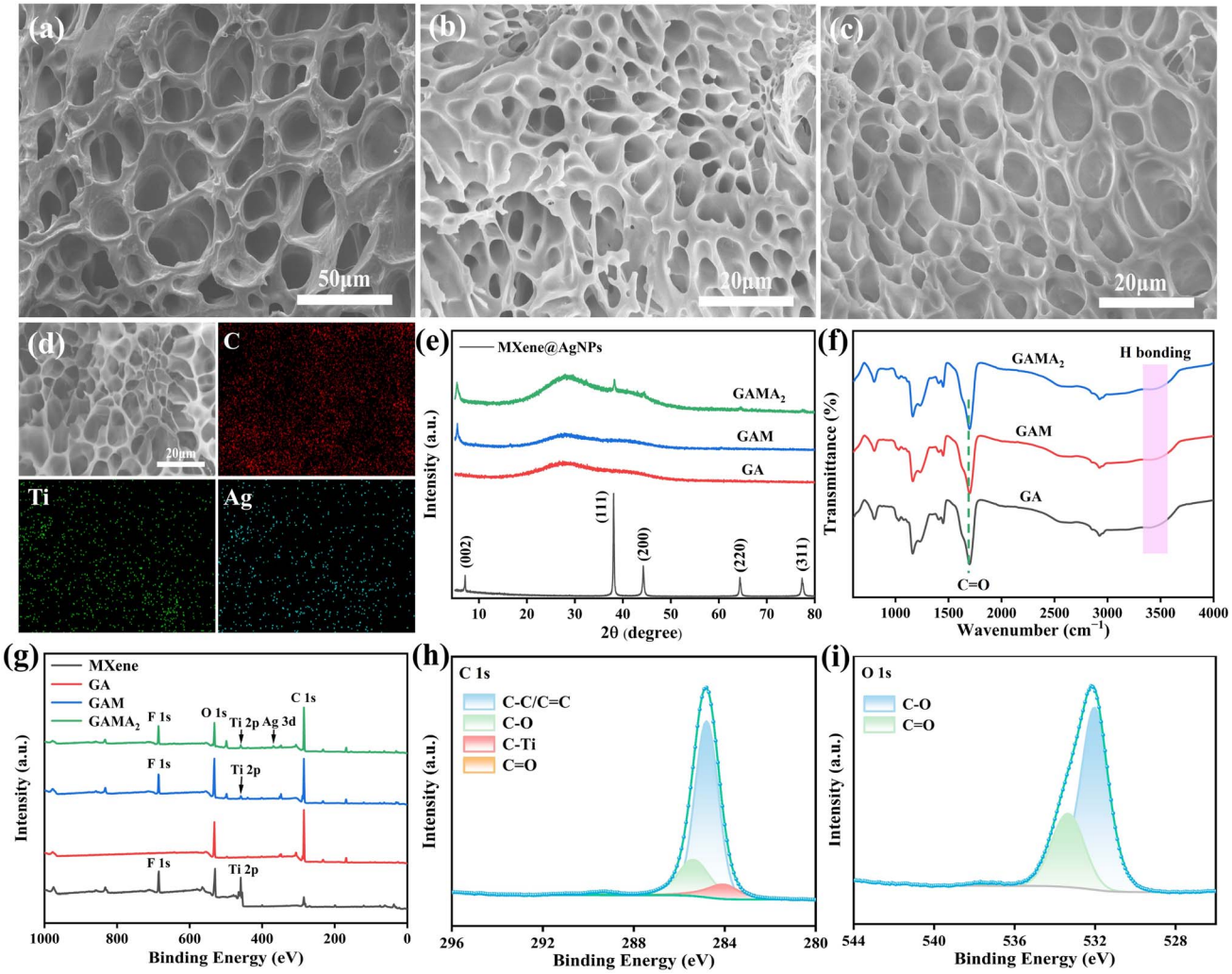

Fig. 2 Material characterizations of GAMA hydrogels. Cross-sectional SEM images of freeze-dried (a) GA hydrogel, (b) GAM hydrogel, and (c) $GAMA_2$ hydrogel. (d) Elemental mapping images of $GAMA_2$ hydrogel. (e) XRD patterns of MXene@AgNPs, pure GA, GAM, $GAMA_2$ hydrogels. (f) FTIR spectra of pure GA, GAM, and $GAMA_2$ hydrogels. (g) XPS spectra of MXene, GA, GAM, $GAMA_2$ hydrogels. (h) C 1s, and (i) O 1s High-resolution XPS spectra $GAMA_2$ hydrogel.

sensitivity of the sensing performance. As shown in Fig. 4a, the $GAMA_2$ hydrogel exhibits excellent adhesion properties to various substrates, including skin, polypropylene (PP), glass, steel, polytetrafluoroethylene (PTFE), and wood. The good adhesion of hydrogels can be ascribed to hydrogen bonding and coordination interactions between the polymer network and the substrate. Multiple binding sites create strong interfacial connections, making the gel adhesive.

To quantitatively evaluate the adhesion strength of the hydrogels, a tensile–shear testing system was used to evaluate the adhesion strength of hydrogels with different conductive fillers added to different substrates. As shown in Fig. 4d, all hydrogel specimens were cut into 20 mm × 20 mm × 4 mm pieces and bonded between two identical substrates. Fig. S7† shows the adhesion–displacement curves of different hydrogels on wood, glass, copper, and PTFE, indicating that the hydrogel exhibits the highest adhesion to wood and the lowest adhesion to glass. As illustrated in Fig. 4b–e, the hydrogel exhibits the highest bonding strength to wood among the four selected substrates. This is primarily attributable to the abundance of hydroxyl and carboxyl groups present on the surface of wood, which facilitate the formation of robust hydrogen bonds and hydrophobic interactions with the hydrogel. Additionally, the dimples on the wood surface enhance the contact area with the hydrogel, thereby intensifying the friction between the hydrogel and the wood.

The adhesion strength of the hydrogel to copper, PTFE, and glass decreased in that order, and the difference in adhesion strength between the different substrates may be due to different interfacial interactions. For copper, the carboxyl groups in the hydrogel formed coordination sites with copper atoms, which promoted the interfacial interactions between the hydrogel and the copper sheet. For PTFE, the adhesion mainly originated from the hydrogen bonding between the hydrogel and PTFE, so the adhesion strength was slightly weaker. For the glass plate, the adhesion strength is mainly determined by the hydrogen bonding between the interfaces and the electrostatic force, but the smooth surface of the glass plate makes the

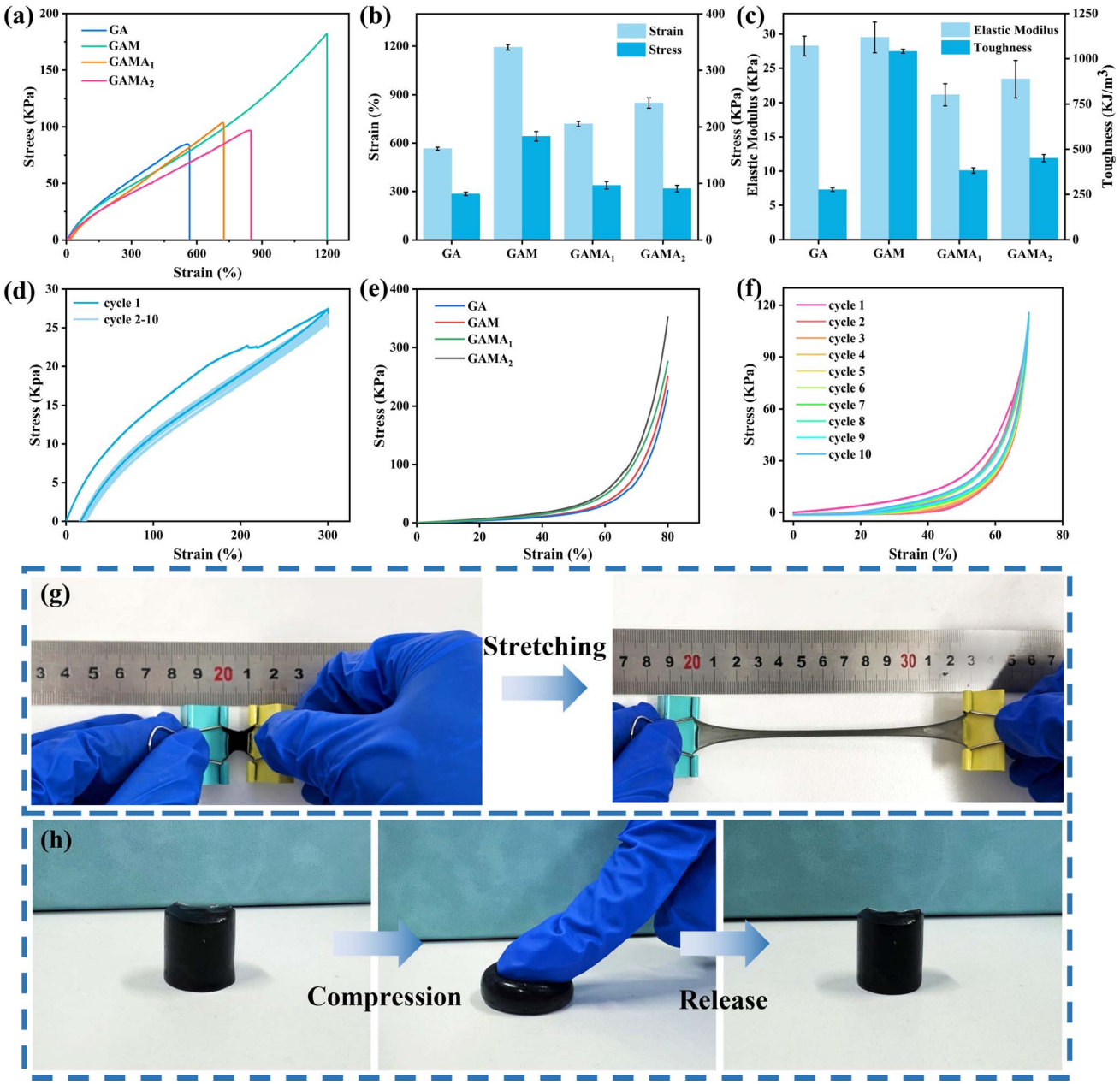

Fig. 3 Mechanical properties of the hydrogels. (a) Stress–strain curves, (b) tensile strain and tensile toughness values, and (c) toughness and modulus of elasticity values of hydrogels with different conductive fillers. (d) Hysteresis curves for 10 stretching–releasing cycles at a strain of 300%. (e) Compressive stress–strain curves of hydrogels with different conductive fillers. (f) Loading and unloading cycle compression curves of $GAMA_2$ hydrogel after 10 cycles at a strain of 70%. Optical photos of (g) large stretching, (h) compressing and recovering.

adhesion strength of the hydrogel to the glass the lowest among the four substrates. Among the four different hydrogels, the adhesion strength of GAM hydrogel to different substrates was the highest. Taking wood as an example, the adhesion strength of GAM hydrogel to wood was 21.5 kPa, which was significantly greater than that of GA hydrogel (13.3 kPa), $GAMA_1$ hydrogel (11.3 kPa) and $GAMA_2$ hydrogel (9.3 kPa). In comparison to pure GA hydrogels, the functional groups on the surface of a significant number of MXene nanosheets in GAM hydrogels are capable of forming hydrogen bonds with the substrate, thereby enhancing the adhesion strength. However, the introduction of MXene@AgNPs into GA hydrogels has resulted in the number of hydrogen bonds formed between the substrate and the hydrogel being reduced due to the presence of a large number of AgNPs on the surface of the MXene. Moreover, AgNPs also form metal–ligand bonds with the hydroxyl groups on the hydrogel surface, which further diminishes adhesion strength.

3.4 Conductivity and electromagnetic shielding properties of hydrogels

To investigate the electromagnetic interference shielding properties of hydrogels, the conductivity was initially

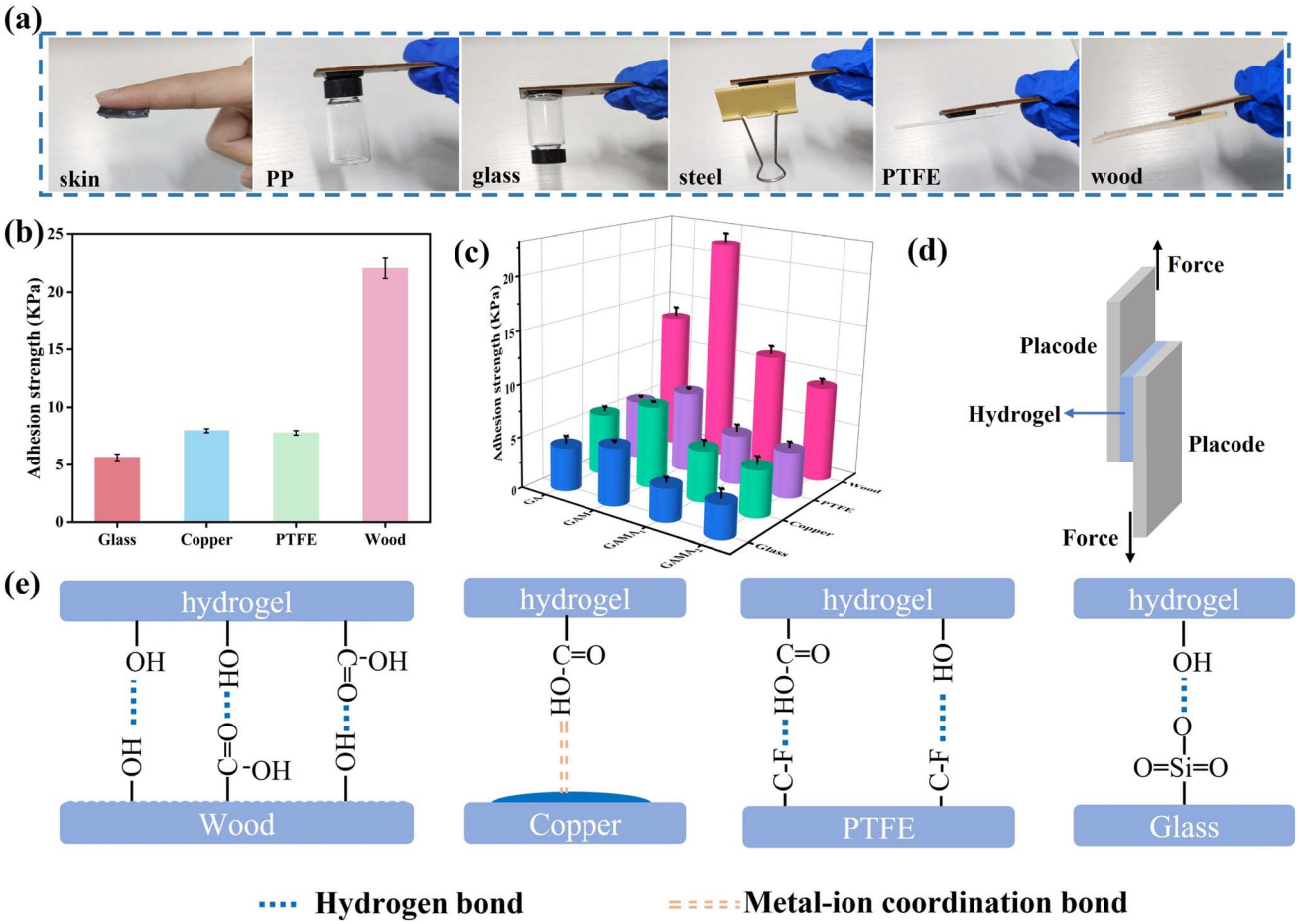

Fig. 4 Adhesion properties of hydrogels. (a) Adhesive performance of the $GAMA_2$ hydrogel to various substrate surfaces at room temperature. (b) The adhesion strength of GAM hydrogel to various substrates. (c) The adhesion strength of hydrogels with different conductive fillers to different substrates. (d) Schematic of the lap shear test. (e) Adhesion mechanisms to various substrates.

measured.[26] The electrical conductivity of GAM and GAMA is derived from the conductive network formed by the uniformly dispersed MXene nanosheets and MXene@AgNPs, respectively. Fig. 5a shows the relationship between the electrical conductivity of the hydrogel and the contents of MXene and AgNPs. With the addition of MXene nanosheets, the conductivity of the hydrogel increased from the insulating state of the pure GA hydrogel to 5.07 mS cm^{-1}. Subsequently, due to the combined effect of MXene nanosheets and AgNPs, the conductivity further increased to 14.04 mS cm^{-1}. The moderate conductivity of the hydrogel is associated with a higher electrical impedance and maintains a considerable attenuation capacity, leading to excellent EMI shielding properties of the hydrogel.[27]

In daily applications, a material with an EMI SE of 20 dB can block about 99% of the incident electromagnetic wave energy.[28] The EMI shielding performance of the hydrogel with a thickness of 4 mm was evaluated by measuring the scattering parameters (S_{11}, S_{12}, S_{21}, and S_{22}) using a vector network analyzer in the frequency range of 8.2–12.4 GHz. Fig. 5b compares the EMI SE values of GA hydrogels with different conductive fillers. The average EMI SE of pure GA hydrogels without any conductive fillers is 21.47 dB, which has reached the commercial 20 dB standard. Notably, the EMI shielding performance of GA hydrogel is mainly attributed to the polarization of water molecules under the influence of electromagnetic fields, as well as the changes in the extensive hydrogen bonding network.[28] With the introduction of MXene nanosheets and MXene@AgNPs composite nanosheets, the average EMI SE of GAM and $GAMA_2$ increased to 24.1 dB and 31 dB, respectively. More importantly, the trend of SE_T variations corresponds to that of conductivity, suggesting that the synergistic interaction between MXene and AgNPs significantly enhances EMI shielding performance.

To evaluate the EMI shielding mechanism of hydrogels, the contributions of absorption loss (SE_A) and reflection loss (SE_R) of hydrogels were analyzed. As illustrated in Fig. 5c, the SE_T and SE_A of $GAMA_2$ hydrogel exhibit a significant growing trend, while the SE_R remains unchanged, demonstrating efficient electromagnetic wave attenuation with composite hydrogels. However, the attenuation of the EMI wave involves reflection first and then absorption. The calculated SE_R is based on the total power of the EMI wave, while the SE_A is based on the power of the incident wave.[29] To further evaluate the actual shielding mechanism of the hydrogel, the transmitted (T), absorbed (A),

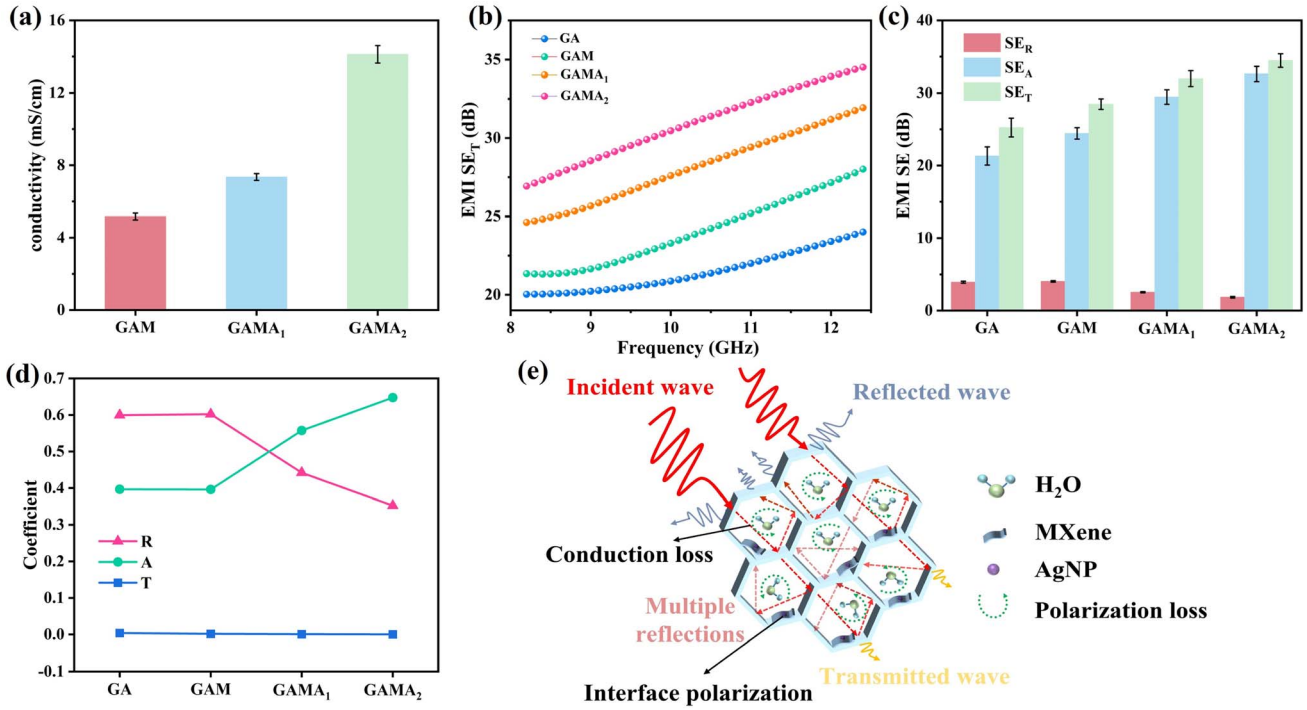

Fig. 5 EMI shielding performance of hydrogels. (a) Electrical conductivity of hydrogels. (b) EMI SE_T of different hydrogels in the frequency range of 8.2–12.4 GHz. (c) The SE_R, SE_A, and SE_T of different hydrogels at 12.4 GHz. (d) *R*–*A*–*T* coefficients of different hydrogels. (e) Scheme showing the EMI shielding mechanism.

and reflected (*R*) power coefficients of the hydrogel are calculated in Fig. 5d. It demonstrates that the *R* of the pure GA hydrogel and GAM hydrogel are greater than the corresponding *A* of the GAM hydrogel. The *R* of pure GA hydrogels and GAM hydrogels are larger than the corresponding *A*, indicating that reflection loss is the predominant shielding mechanism. Furthermore, the *R* of GAM hydrogels are slightly larger than those of pure GA hydrogels, which is mainly due to the inevitable increase in impedance matching and electromagnetic wave reflection resulting from the incorporation of MXene nanosheets. The incorporation of MXene@AgNPs into the hydrogel results in an *A* greater than the *R*, indicating that the synergistic effect of MXene nanosheets and AgNPs promotes absorption rather than reflection. Furthermore, the power coefficient *A* increases as the content of AgNPs rises, while the *R* shows an opposite trend, suggesting that AgNPs enhance the hydrogel's absorption capability. In general, reflection attenuation is dependent on impedance mismatch at the interface between air and the shielding material. In contrast, absorption attenuation is associated with electromagnetic energy conversion, which is facilitated by induced currents and polarization relaxation.[30–32]

Fig. 5e illustrates the EMI shielding mechanism of the $GAMA_2$ hydrogel. The incident electromagnetic waves are partially reflected, and only a small portion of the waves can penetrate through the hydrogel. The remaining electromagnetic waves are absorbed inside the $GAMA_2$ hydrogel and converted into heat energy and dissipation.[33] The absorption effect arises from the conductive loss caused by the conductive network formed by MXene/AgNPs, the dipolar polarization loss due to abundant functional groups and defects, and the interfacial polarization loss caused by rich heterogeneous interfaces. Additionally, the porous structure increases multiple reflections of the electromagnetic waves, which prolongs the propagation path of the incident waves and enhances the absorption effect. In summary, the excellent EMI shielding performance of $GAMA_2$ is the result of the synergistic effects of multiple reflections, conductive loss, and polarization loss.[34,35]

3.5 Sensing properties of $GAMA_2$ hydrogel

Due to its excellent tensile properties and conductivity, the porous $GAMA_2$ hydrogel experiences changes in resistance under stress, thereby enabling the monitoring of human motion. In order to evaluate the potential of $GAMA_2$ hydrogel as a flexible strain sensor, the relationship between its relative resistance with tensile strain was investigated. As illustrated in Fig. S8,† during the slow stretching of the hydrogel, the brightness of the light bulb gradually dimmed, which indicates that the stretching strain leads to an increase in the resistance of the hydrogel. Therefore, the strain sensitivity of the $GAMA_2$ hydrogel as a strain sensor can be determined by fitting the slope of the resistance–strain curve during stretching. As shown in Fig. 6a, the $GAMA_2$ hydrogel exhibits a gauge factor (GF) of 2.06 in the 0–100% strain range and 3.42 in the 100–200% strain range. Furthermore, the hydrogel demonstrates a GF of 6.4 in the 200–300% strain range. Overall, the hydrogel exhibits a substantial linear operating range and notable sensitivity,

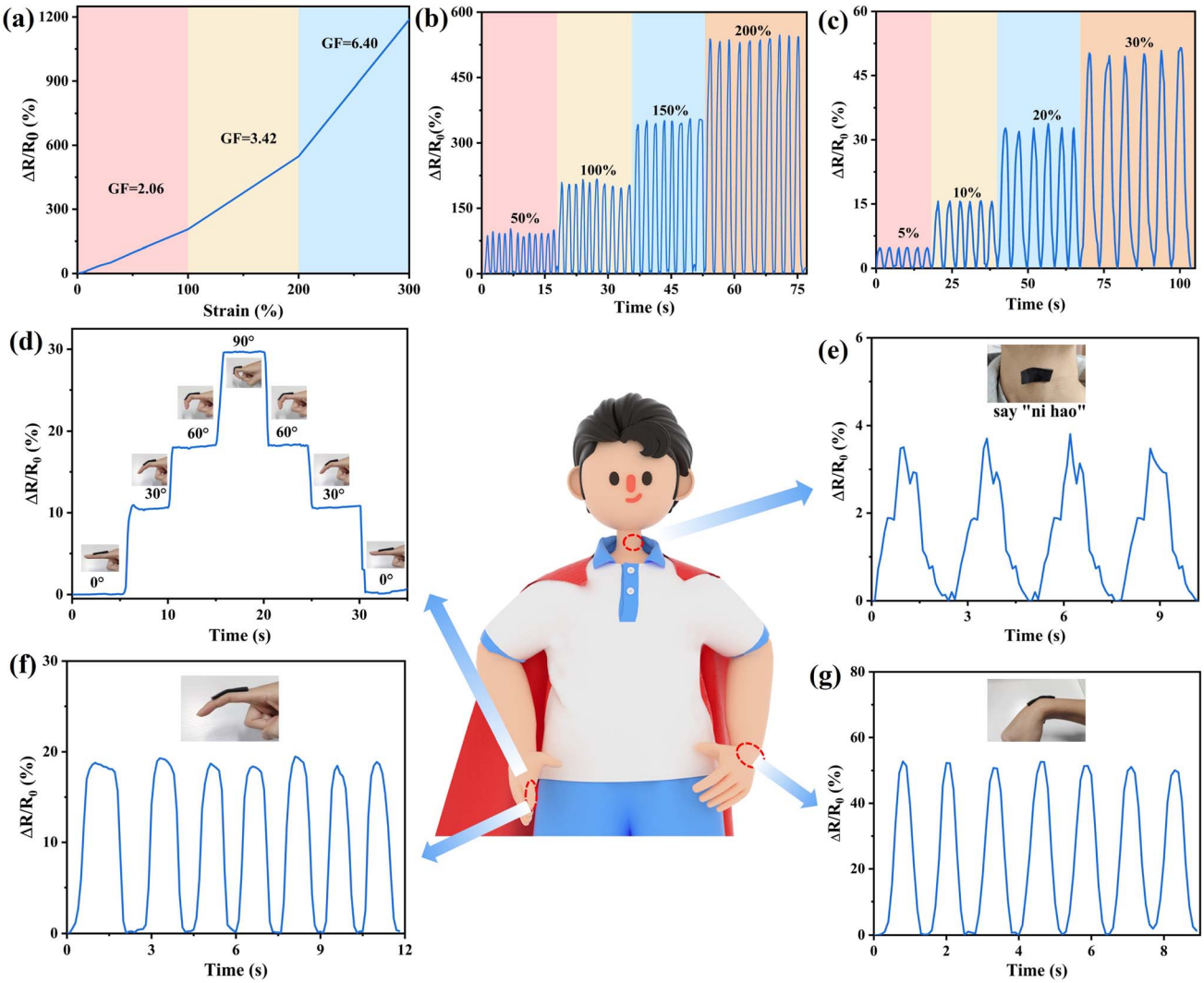

Fig. 6 Sensing performance of the $GAMA_2$ hydrogel sensor. (a) GF of the $GAMA_2$ hydrogel sensor at different strains. (b) Real-time response signals of the $GAMA_2$ hydrogel sensor toward large strains (50%, 100%, 150%, and 200%). (c) Real-time response signals of the $GAMA_2$ hydrogel sensor toward subtle strains (5%, 10%, 20%, and 30%). Resistance responses of the sensor toward: (d) finger bending at different angles (0°, 30°, 60°, and 90°); (e) voice recognition speaking "ni hao"; (f) continuous finger bending and (g) continuous bending of the wrist.

which are superior to that of previously reported hydrogel-based strain sensors.[36,37] The strain-sensing response of the $GAMA_2$ hydrogel stems from the changes in the electron transport pathways within the MXene nanosheet network during stretching. Additionally, the change to the three-dimensional interconnected porous structure promotes ion migration within the hydrogel. Therefore, the hydrogel can accurately detect tensile deformations of varying magnitudes. Notably, the relative change in resistance increases with tensile strain over a wide range of 5–200%, indicating that the strain sensor has a broad operational range, along with excellent responsiveness and repeatability (Fig. 6b and c).

Furthermore, owing to its remarkable adhesion properties, the hydrogel can be directly affixed to human skin for real-time monitoring of fingers, wrists, throat, and other areas. As illustrated in Fig. 6d–g, as the bending angle of a finger increases from 0° to 90°, the relative resistance signal gradually rises due to slight stretching of the hydrogel strain sensor. Conversely, when the finger is maintained at a fixed bending angle, the relative resistance remains stable, indicating that the resistance increases with strain on the hydrogel. The stability of the relative resistance further suggests that the hydrogel has high consistency and stability. Notably, when the bending angle is varied from 0° to 90° and then back to 0°, the relative resistance changes consistently, demonstrating that the hydrogel sensor is capable of transiently detecting finger movements. Additionally, due to its high sensitivity, the hydrogel sensor can monitor small body movements. When placed on a volunteer's throat, the sensor shows regular and reproducible changes in relative resistance as the volunteer "repeatedly says "ni hao". These results suggest that hydrogel sensors can serve as multifunctional wearable flexible sensors, which can quickly and accurately monitor various body movements and speech recognition.

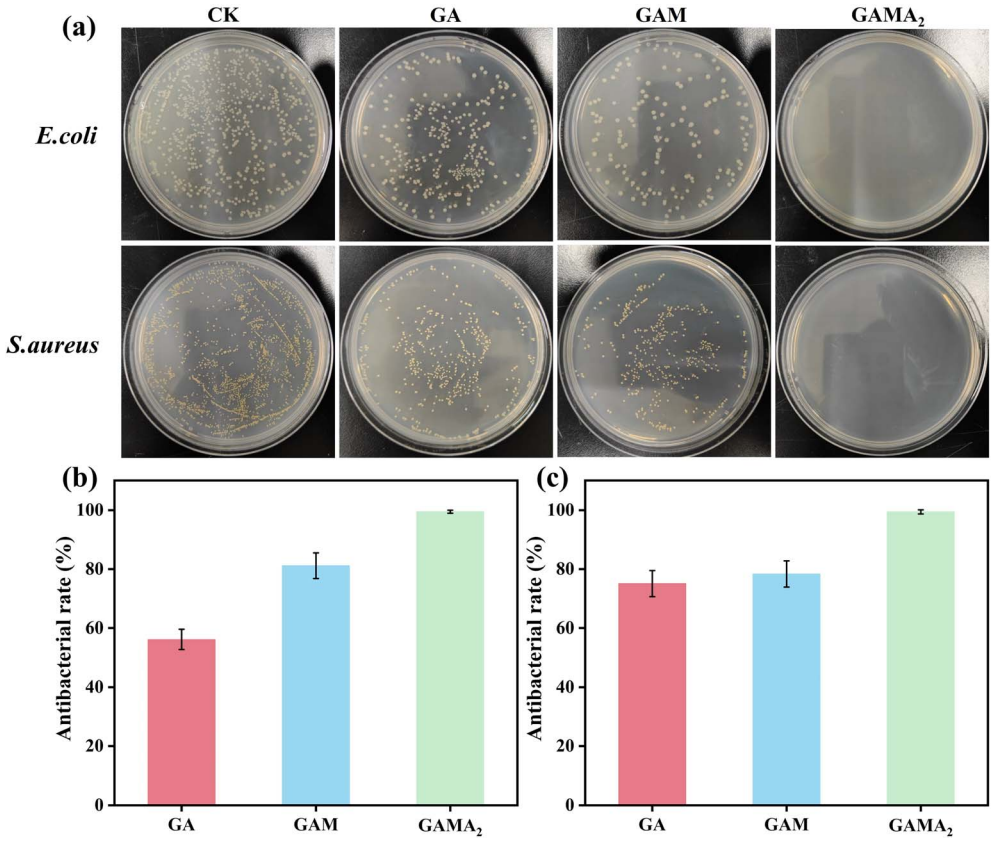

Fig. 7 Antibacterial performance of the $GAMA_2$ hydrogel. (a) Photographs of the flat colony counting method for GA, GAM and $GAMA_2$ hydrogels against *E. coli* and *S. aureus*. (b) Antibacterial rate of the hydrogels against *E. coli*. (c) Antibacterial rate of the hydrogels against *S. aureus*.

3.6 Antimicrobial properties of $GAMA_2$ hydrogel

Wearable hydrogel sensors attached to human skin are susceptible to bacterial growth, which not only compromises the normal functionality of the hydrogel but also endangers human health.[38] Accordingly, the antimicrobial properties of the $GAMA_2$ hydrogel were evaluated against *Escherichia coli* (a Gram-negative bacterium) and *Staphylococcus aureus* (a Gram-positive bacterium) using a plate colony counting method. By introducing differently doped hydrogels into the bacterial solution, varying colony counts could be observed. As illustrated in Fig. 7a–c, the inhibition rate of GA hydrogel on *E. coli* and *S. aureus* was 56.91% and 74.97%, respectively. The GAM hydrogel containing MXene nanosheets exhibits stronger inhibition against *E. coli* and *S. aureus*, with inhibition rates increasing to 81.45% and 78.83%, respectively. Furthermore, thanks to the potent antibacterial effect of AgNPs, the $GAMA_2$ hydrogel demonstrates exceptional antimicrobial activity, with an antibacterial rate of 100% against both *E. coli* and *S. aureus*.

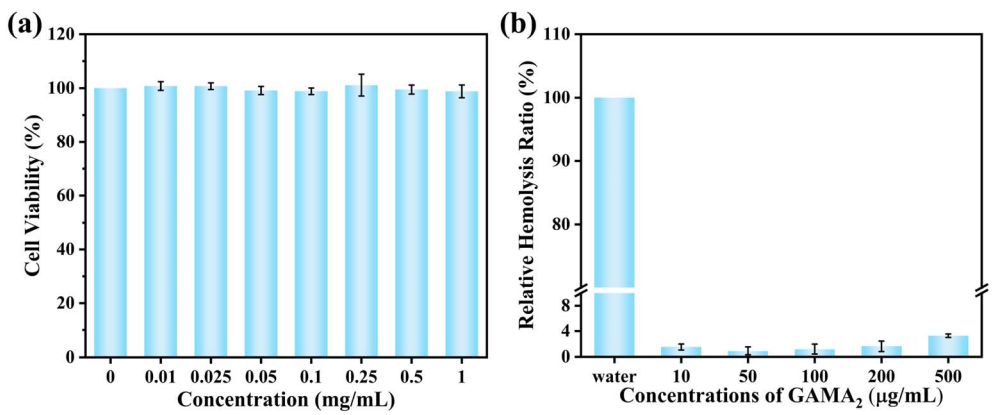

Fig. 8 Biocompatibility of $GAMA_2$ hydrogel. (a) Cell viability detected by CCK-8 assay after 24 h of treatment. (b) Hemolysis ratio analysis.

3.7 Biocompatibility of $GAMA_2$ hydrogel

In addition to antibacterial activity, biocompatibility and biosafety are crucial for antibacterial hydrogels.[39] Therefore, the biocompatibility and biosafety of $GAMA_2$ hydrogel were systematically evaluated. First, the CCK-8 assay was used to assess the effect of $GAMA_2$ hydrogel on the viability of human fibroblasts. As shown in Fig. 8a, within the concentration range of 0.01–1 mg mL^{-1}, $GAMA_2$ hydrogel did not exhibit any toxicity to the cells, and the cell viability in each concentration group was maintained above 98%. This indicates that the extracts of $GAMA_2$ hydrogel have good cytocompatibility with human fibroblasts within the tested concentration range. Next, an *in vitro* hemolysis assay was conducted to explore the blood compatibility of $GAMA_2$ hydrogel. As shown in Fig. 8b, even when the concentration of $GAMA_2$ reached 500 μg mL^{-1}, the hemolysis rate caused by $GAMA_2$ hydrogel was 3.26%, indicating that $GAMA_2$ hydrogel has good blood compatibility.

4 Conclusion

In summary, we developed a GAMA hydrogel. The multifunctional conductive filler MXene@AgNPs were prepared by *in situ* reduction of $AgNO_3$ using MXene nanosheets, and then it was introduced into the GG/AA dual-network structure. This hydrogel exhibited excellent stretchability, self-adhesion, efficient EMI shielding, sensing, antibacterial capability and biocompatibility. The good interfacial interaction between MXene and GA hydrogels guarantees the structural stability of the GAM hydrogel, with a tensile strength of 181 kPa at 1200% strain. Although the incorporation of MXene@AgNPs occupies part of the polymer functional groups, the composite hydrogel still maintains excellent self-adhesion properties. Coupled with the conductive loss and polarization loss induced by MXene@AgNPs, as well as the multiple reflection losses generated by the porous structure, the composite hydrogel exhibits an efficient EMI SE of 34.5 dB in the X-band. Moreover, due to its outstanding strain and conductivity performance, the GAMA hydrogel functions as a highly sensitive and reliable wearable sensor for human motion monitoring. Meanwhile, comprehensive biocompatibility evaluations have confirmed its excellent antibacterial performance, hemocompatibility, and cytocompatibility. Overall, the well-designed GAMA hydrogel integrates and balances multiple functionalities. The GAMA hydrogel demonstrates vast potential in wearable healthcare, flexible electronics, and biomedical engineering. By its multifunctional design, the current GAMA hydrogel is poised to expand its applications to dynamic health monitoring systems, smart wound dressings, protective coatings for implantable devices, as well as flexible electronics and soft robotics.

Data availability

The datasets generated and analyzed in this current study are available from the corresponding author upon reasonable request.

Author contributions

Tongle Pu: writing–original draft, review & editing, visualization, formal analysis, data curation. Changgeng Li: investigation, methodology, resources. Lin Yang: visualization, validation, investigation. Xiu-zhi Tang: funding acquisition, resources, supervision. Yunjun Ruan: funding acquisition, resources, supervision. Tong Guo: funding acquisition, resources, supervision, project administration.

Conflicts of interest

No conflict of interest exists in the submission of this manuscript, and the manuscript is approved by all authors for publication. I would like to declare on behalf of my co-authors that the work described was original research that has not been published previously and is not under consideration for publication elsewhere, in whole or in part. All the authors listed have approved the manuscript that is enclosed.

Acknowledgements

The authors are grateful for the financial support from the Natural Science Special (Special-term Professor) Research Foundation of Guizhou University (Grant No. [2021]23), the cultivation project of Guizhou University (Grant No. [2020]16) and the Guizhou Provincial Science and Technology Projects (Grant No. ZK [2022]52). Moreover, the work was supported by the Industry and Education Combination Innovation Platform of Intelligent Manufacturing and Graduate Joint Training Base at Guizhou University (Grant No. 2020-520000-83-01-324061) and Construction of Science and Technology Platform of Guiyang (Grant No. [2023]7-3).

References

1 K. Chen, K. Liang, H. Liu, R. Liu, Y. Liu, S. Zeng and Y. Tian, *Nano-Micro Lett.*, 2023, **15**, 102.
2 D. Lu, M. Zhu, X. Li, Z. Zhu, X. Lin, C. F. Guo and X. Xiang, *J. Mater. Chem. A*, 2023, **11**, 18247–18261.
3 X. Li, L. He, Y. Li, M. Chao, M. Li, P. Wan and L. Zhang, *ACS Nano*, 2021, **15**, 7765–7773.
4 J. Wu, Q. Ma, Q. Pang, S. Hu, Z. Wan, X. Peng, X. Cheng and L. Geng, *Carbohydr. Polym.*, 2023, **321**, 121282.
5 Y. Xie, X. Shi, S. Gao, C. Lai, C. Lu, Y. Huang, D. Zhang, S. Nie, F. Xu and F. Chu, *J. Mater. Chem. A*, 2024, **12**, 5124–5132.
6 J. Qu, Q. Yuan, Z. Li, Z. Wang, F. Xu, Q. Fan, M. Zhang, X. Qian, X. Wang, X. Wang and M. Xu, *Nano Energy*, 2023, **111**, 108387.
7 J. Jiang, S. Xu, H. Ma, C. Li and Z. Huang, *Mater. Today Bio*, 2023, **20**, 100657.
8 Q. Li, B. Tian, J. Liang and W. Wu, *Mater. Chem. Front.*, 2023, **7**, 2925–2957.
9 Z. Qin, Y. Li, X. Wang, Y. Liu, N. Li, Q. Xu, L. Ye and T. Jiao, *J. Mater. Chem. A*, 2024, **12**, 10808.

10 Z. Nie, K. Peng, L. Lin, J. Yang, Z. Cheng, Q. Gan, Y. Chen and C. Feng, *Chem. Eng. J.*, 2023, **454**, 139843.
11 C. Chen, S. Qiu, M. Cui, S. Qin, G. Yan, H. Zhao, L. Wang and Q. Xue, *Carbon*, 2017, **114**, 356–366.
12 W. Zhang, P.-L. Wang, L.-Z. Huang, W.-Y. Guo, J. Zhao and M.-G. Ma, *Nano Energy*, 2023, **117**, 108875.
13 R. Zhang, D. Xie, C. Zhang, Z. Xu, Y. Fang, W. Wang, M. Xu and Y. Song, *J. Mater. Chem. A*, 2023, **11**, 24608–24617.
14 H. Zhong, Y. Fang, M. Luo, L. Wang, J. Huang, G. Dai, K. Liu, J. Wu and J. Du, *ACS Appl. Mater. Interfaces*, 2024, **16**, 28209–28221.
15 L. T. Gao, Y. M. Chen, Y. Aziz, W. Wei, X. Y. Zhao, Y. He, J. Li, H. Li, H. Miyatake and Y. Ito, *Carbohydr. Polym.*, 2024, **330**, 121812.
16 T. Chen, X. Li, Q. Wang, Y. Li, L. Xu, Y. Yang, Y. Qiao, Y. Dai, J. Ke, H. Wan, S. Zhou and Z. Gao, *Int. J. Biol. Macromol.*, 2024, **270**, 132035.
17 X. Zhang, K. Liu, M. Qin, W. Lan, L. Wang, Z. Liang, X. Li, Y. Wei, Y. Hu, L. Zhao, X. Lian and D. Huang, *Carbohydr. Polym.*, 2023, **309**, 120702.
18 X. Nie, Y. Xie, X. Ding, L. Dai, F. Gao, W. Song, X. Li, P. Liu, Z. Tan, H. Shi, C. Lai, D. Zhang and Y. Lai, *Carbohydr. Polym.*, 2024, **334**, 122068.
19 F. Gao, Y. Pang, Y. Wang, X. Yang, W. Song, X. Nie, Z. Tan, J. Zhou, Y. Xin, D. Wang, H. Shi, C. Lai and D. Zhang, *ACS Sustain. Chem. Eng.*, 2024, **12**, 13622–13633.
20 K. Elkhoury, M. Morsink, L. Sanchez-Gonzalez, C. Kahn, A. Tamayol and E. Arab-Tehrany, *Bioact. Mater.*, 2021, **6**, 3904–3923.
21 Y. Huang, L. Mu, X. Zhao, Y. Han and B. Guo, *ACS Nano*, 2022, **16**, 13022–13036.
22 C. Liu, Z. Xu, S. Chandrasekaran, Y. Liu and M. Wu, *Carbohydr. Polym.*, 2023, **303**, 120468.
23 W. Kong, Z. Wang, M. Wang, K. C. Manning, A. Uppal, M. D. Green, R. Y. Wang and K. Rykaczewski, *Adv. Mater.*, 2019, **31**, 1904309.
24 Z. Deng, Y. Guo, X. Zhao, P. X. Ma and B. Guo, *Chem. Mater.*, 2018, **30**, 1729–1742.
25 H. Fang, J. Wang, L. Li, L. Xu, Y. Wu, Y. Wang, X. Fei, J. Tian and Y. Li, *Chem. Eng. J.*, 2019, **365**, 153–164.
26 R. Zhang, D. Xie, C. Zhang, Z. Xu, Y. Fang, W. Wang, M. Xu and Y. Song, *J. Mater. Chem. A*, 2023, **11**, 24608–24617.
27 Y. Yang, B. Li, N. Wu, W. Liu, S. Zhao, C. J. Zhang, J. Liu and Z. Zeng, *ACS Mater. Lett.*, 2022, **4**, 2352–2361.
28 S. Gong, X. Sheng, X. Li, M. Sheng, H. Wu, X. Lu and J. Qu, *Adv. Funct. Mater.*, 2022, **32**, 2200570.
29 M. H. Al-Saleh, W. H. Saadeh and U. Sundararaj, *Carbon*, 2013, **60**, 146–156.
30 Y. Yang, S. Chen, W. Li, P. Li, J. Ma, B. Li, X. Zhao, Z. Ju, H. Chang, L. Xiao, H. Xu and Y. Liu, *ACS Nano*, 2020, **14**, 8754–8765.
31 Z. Wu, K. Pei, L. Xing, X. Yu, W. You and R. Che, *Adv. Funct. Mater.*, 2019, **29**, 1901448.
32 Q. Liu, X. Liu, H. Feng, H. Shui and R. Yu, *Chem. Eng. J.*, 2017, **314**, 320–327.
33 W. Yang, B. Shao, T. Liu, Y. Zhang, R. Huang, F. Chen and Q. Fu, *ACS Appl. Mater. Interfaces*, 2018, **10**, 8245–8257.
34 A. Iqbal, F. Shahzad, K. Hantanasirisakul, M.-K. Kim, J. Kwon, J. Hong, H. Kim, D. Kim, Y. Gogotsi and C. M. Koo, *Science*, 2020, **369**, 446–450.
35 Y. Zhang, Y. Huang, T. Zhang, H. Chang, P. Xiao, H. Chen, Z. Huang and Y. Chen, *Adv. Mater.*, 2015, **27**, 2049–2053.
36 Q. Wang, Q. Zhang, G. Wang, Y. Wang, X. Ren and G. Gao, *ACS Appl. Mater. Interfaces*, 2022, **14**, 1921–1928.
37 G. Huang, P. Wang, Y. Cai, K. Jiang and H. Li, *J. Polym. Sci.*, 2023, **61**, 1675–1687.
38 Q. Xu, M. Hou, L. Wang, X. Zhang and L. Liu, *Chem. Eng. J.*, 2023, **477**, 147065.
39 P. Xin, S. Han, J. Huang, C. Zhou, J. Zhang, X. You and J. Wu, *Chin. Chem. Lett.*, 2023, **34**, 108125.